Research Article | Vol. 1, No. 4 | 15 Dec 2018 | OSA CONTINUUM 1226
OSA CONTINUUM

Study of wavelength switching time in tunable semiconductor micro-ring lasers: experiment and travelling wave description

MULHAM KHODER,[1,*] MINDAUGAS RADZIUNAS,[2,3] VASILE TRONCIU,[4] AND GUY VERSCHAFFELT[5]

[1]*Brussels Photonics (B-PHOT), Department of Applied Physics and Photonics, Vrije Universiteit Brussel, Pleinlaan 2, B-1050 Brussels, Belgium*
[2]*Weierstrass Institute for Applied Analysis and Stochastics Leibniz Institute in Forschungsverbund Berlin e.V., Mohrenstrasse 39, 10117 Berlin, Germany*
[3]*MQ Photonics Research Centre and Department of Physics and Astronomy, Macquarie University, Sydney, NSW 2109, Australia*
[4]*Department of Physics, Technical University of Moldova, bd. Stefan cel Mare 168, Chisinau MD-2005, Moldova*
[5]*Applied Physics Research Group (APHY), Department of Applied Physics and Photonics, Vrije Universiteit Brussel, Pleinlaan 2, B-1050 Brussels, Belgium*
[*]*mulham.khoder@vub.be*

Abstract: We report in this paper the wavelength switching features of semiconductor ring lasers that are wavelength tunable based on filtered optical feedback. The filtered feedback provides a wavelength dependent loss mechanism in these devices with which a particular longitudinal mode, and thus a particular wavelength, can be selected by changing the filter characteristics of the feedback channel. We investigate how the wavelength switching speed depends on the amplitude of the modulation of the switching driving signal and on the different phase factors within the filtering branches of the SRL. We compare qualitatively the experimental results with numerical simulations based on a travelling wave model. We also investigate the dynamical behavior of the lasing and nonlasing longitudinal modes in the two channels of the clockwise and the counter-clockwise directions. We show the crucial importance of various phase relation factors on the wavelength switching behavior. Finally, we discuss what limits the switching speed and how we can accelerate it.

1. Introduction

Wavelength tunable lasers [1] are being used in several applications, such as optical sensing [2] and wavelength division multiplexing [3]. Therefore, during last years there is a large interest in the further development and optimization of such tunable lasers. There exist many different approaches in order to make a tunable laser, each approach having its particular advantages and disadvantages. These approaches typically rely on changing the laser's effective cavity length [4], by varying the physical length of the cavity or its refractive index, or by introducing a wavelength dependence in the cavity such as in the arrayed waveguide grating lasers [5].

Filtered optical feedback (FOF) is one way of achieving a laser with controllable wavelength. In this approach, part of the light emitted by the laser is reinjected in the cavity after passing through a wavelength dependent optical filter. If the reinjected light has the same phase as the originally emitted field and if the delay is short (compared to the relaxation oscillations time scale), the filtered feedback will select those laser mode(s) whose wavelength is closest to the transmission maximum of the filter in the feedback section [6]. The wavelength selective elements in such tunable lasers are thus placed outside of the laser cavity, which can have a positive effect on the stability of the selected wavelength [7] and can result in a simpler control system

#341184 https://doi.org/10.1364/OSAC.1.001226
Journal © 2018 Received 31 Jul 2018; revised 24 Oct 2018; accepted 26 Oct 2018; published 30 Nov 2018

OSA CONTINUUM

needed to tune the emitted wavelength [8]. This approach has been implemented successfully in a number of laser architectures. For example, FOF has been used to make a tunable Fabry-Perot semiconductor laser in [9] and a tunable semiconductor ring laser in [10]. In both papers the filtered feedback section has been fabricated on the same chip as the laser, which results in a compact, robust and potentially low-cost device. In [9], the strength of the FOF is controlled by adjusting the current send through semiconductor optical amplifiers (SOAs). In [10], a switching time of 450 ps between adjacent wavelengths has been achieved in SRLs using on-chip FOF which is controlled by electrically pumped distributed Bragg reflectors.

In our previous works, we have combined the electrical control of the FOF from [9] with semiconductor ring lasers (SRLs). SRLs have attracted interest experimentaly and theortically [11–13] due to their directional bistability which makes it possible to operate these lasers in either of the two counter-propagating directions [14, 15]. It is also possible to optically trigger a switch between these directional modes, which can be used to realise an all-optical flip-flop based on SRLs [16, 17]. Several studies have proposed to use ring lasers in order to reduce the sensitivity to external feedback [18] as SRL can already exhibit reduced sensitivity to external feedback even in the absence of any special procedures, due to intrinsic bistability with respect to clockwise (CW) and counterclockwise (CCW) operation [19]. This sensitivity to external feedback can be reduced more using a one-sided strong reflector [20], or by using a second controlled feedback [21]. In [22], FOF has been used to reduce the SRL sensitivity to external optical injection.

On chip FOF has been used in SRLs in order to obtain tunable single mode emission [8, 23], controllable multi-wavelength emission [24, 25] and to decrease the sensitivity of SRL against (undesired) external feedback [21, 26]. We have also shown that the switching from one wavelength to another is rather fast (ns time scale) and is governed by a short transition time together with a non-negligable (longer) delay time at each switching event [27]. However, it is important to know the parameters which control the wavelength switching time.

In this paper we investigate in details the effect of the FOF and the amplitude of the modulation of the switching driving signal on the wavelength switching speed in SRLs. We numerically illustrate that different switching scenarios can take place in SRLs. We start in Section 2 by describing the laser and experimental setup. In section 3 the experimental results are presented. We show the effect of the modulation amplitude (of the SOA gates in the feedback loop) on both the transition and the delay time. In Section 4, numerically simulated results based on a traveling wave model are shown. Finally, the summary and conclusions are given in Section 5.

2. Device description and experimental setup

The SRL and the filtered feedback section are fabricated on the same chip by the JePPIX platform [28]. Details of the fabrication and the layout can be found in [23]. A microscopic photo of the device is shown in Fig. 1 (top). The ring cavity of the SRL has a race-track geometry with two straight active waveguides, 753 μm long each, connected to each other via two passive, curved waveguides with a bend radius of 107 μm. The circumference of the ring defines the mode spacing.

The filtered feedback section includes two identical arrayed-waveguide gratings (AWGs) filters with one input connected to the SRL and four outputs which are mutually connected. This provides self-feedback, i.e. each directional mode of the ring will be re-injected in itself after a round-trip in the filtered feedback section. Both ends of the of outcoupling waveguide were tilted in order to reduce the facet reflectivity. To achieve some asymmetry between CW and CCW fields, we applied an additional anti-reflection coating to one of the facets (the left side of the chip (see top panel of Fig. 1) while the right side was left as cleaved.

The AWGs in the feedback section are used to split the SRL light into 4 different wavelength channels. We have chosen to make the AWG filter channels broader than the longitudinal mode

OSA CONTINUUM

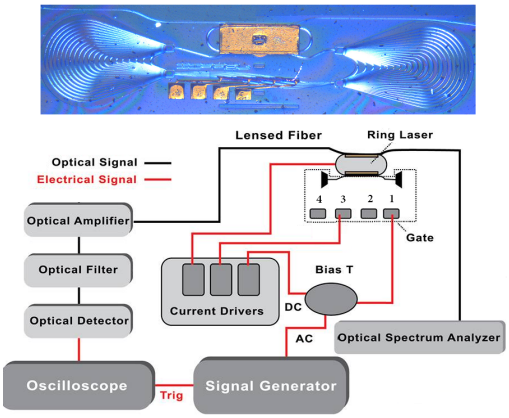

Fig. 1. Top: Microscopic image of the device, bottom: Schematic of the lab setup.

(LM) spacing, because otherwise there is a risk that, due to fabrication tolerances, the LMs are spectrally positioned far from the filter transmission maxima. The AWG channel spacing is 1.336 nm (166.92 GHz) and the AWG free spectral range is 5.65 nm, whereas the LM spacing is chosen to be 0.3 nm. Four electrically controllable SOAs gates are located in the middle of the four waveguides that are used to connect the two AWGs with each other. Each gate can be independently pumped with an electrical bias current using a metalic contact pad. When a gate is biased, the feedback strength and phase of the LMs (in the corresponding AWG channel) change while there is only a small residual feedback or no feedback at all without bias or for a reverse bias of the SOA.

We use the setup that is schematically illustrated in Fig. 1 (bottom) in order to test the tunable SRL. The temperature of the laser's mount is stabilized at 21°C. We use three electrical probes to provide current to different parts of the device: one probe is used to pump the SRL, a second one is used to pump one of the SOA gates (i.e. gate 1 in Fig. 1) and the third probe is connected to another SOA gate (i.e. gate 3 in Fig. 1). The SRL output in the CW and CCW directions is collected using lensed fibers.

3. Experimental study of SRL switching

We start by checking the output power of the SRL in the two directional modes (without feedback) when we increase the pumping current of the SRL. We notice that the threshold current of the device is I_{SRL} =64.5 mA. By further increasing the injected current in the SRL, the output power in both directions is irregular. The SRL is bidirectional for all the currents above the threshold. It emits in the two directions with more power in the CW direction than the CCW direction. We used the oscilloscope to measure time traces of the device's output. We did not notice the alternate oscillation regime in this SRL. The bidirectional output of our device indicates that the backscattering is the dominant coupling mechanism between the CW and CCW modes while the difference in the power between the CW and the CCW directions can be understood due to the asymmetry introduced by using anti-coating reflection on one side of the chip while the other side was left as cleaved.

We investigate the optical spectrum of our device by using the setup shown in Fig. 1 (bottom). The output of the laser is single mode when the pumping current is close to the threshold. By increasing the pumping current and starting from 80 mA, the output of the laser becomes multimode as is for example shown in the spectrum, shown in Fig. 2, of the CW mode when the laser is pumped at 85 mA and without pumping any gate. A similar spectrum has been observed

OSA CONTINUUM

in the CCW direction. In [23], it has been shown that using FOF, the multimode emission can be changed to a single mode in a controlled way. In this work, we need the FOF in order to achieve single mode emission such that we can measure the wavelength switching speed when the laser switches to another (single) mode.

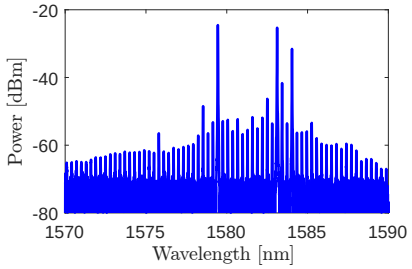

Fig. 2. Optical spectrum of the output of the SRL in the CW direction when it is pumped at 85 mA and without pumping any gate (without feedback).

The strength of the FOF depends on the current injected in the SOAs. For this reason we need to estimate the amplification of the SOA. we use an identical SOA of another device on the same chip with our device (because the SOAs in our device is not accessible for a direct measurement). In the device which is used for characterization of the SOA, the light after being amplified by the SOA passes through a waveguide until it reaches the chip facet as can be seen in Fig. 3 (left) where we show the setup to measure the amplification of the SOA gate. A current driver is used to pump the SOA while its output is collected using a lensed fiber which is connected to a splitter which divides the output to two sections, one is connected to a power meter and the other section is connected to an optical spectrum analyzer (OSA). We increase the current which is applied on the SOA using a current driver and we measure the output power as a function of the injected current into the SOA. The results are shown in Fig. 3 (right). In this figure, we see that the output power increases from 2 nW to 115 nW when the current in the SOA increases from 0 to 50 mA. Above approximately 30 mA, the output power from the SOA seems to saturate. On the optical spectrum analyzer which is shown in the setup scheme in [in Fig. 3 (left)], we do not observe any signature in the optical spectrum; that suggests lasing in the output waveguide due to the pumping of the SOA gate.

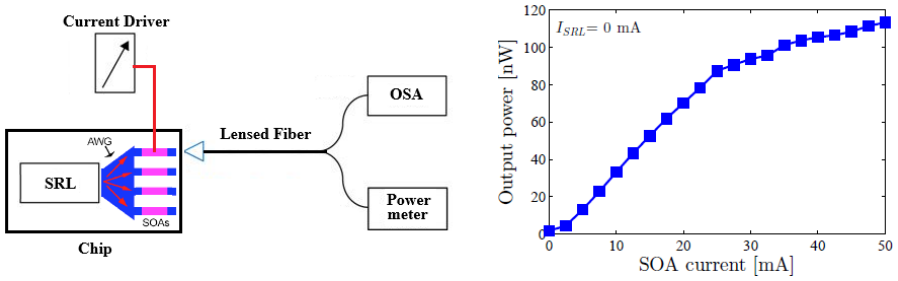

Fig. 3. (left) A schematic representation of the test structure which is used to characterize the SOA gate. (Right) Output power of the SOA amplifier as a function of the injection current (when the SRL is switched off).

By tuning the currents I_1, I_2, I_3, I_4 injected in the SOA gates, we can control the emission wavelength. For more details on such characteristics of the SRL see [23, 33]. We apply a fixed current of 95 mA to the SRL. If we pump gate 1 at 14.2mA ,the SRL emits a single LM at λ_1 =

OSA CONTINUUM

1581.048 nm. This LM is positioned within the passband of gate 1 channel. The corresponding optical spectrum in the CW direction is shown in Fig. 4 The SRL will emit the same wavelength even if we applied a current equal or less than 3.55mA on gate 3. By increasing the pump current of gate 3 to between 3.55mA and less than 38mA, the SRL' s output is multimode. By further increasing the pump current of gate 3 to 38 mA, the SRL' s output switches from the LM at λ_1 to the LM at λ_3 = 1583.790 nm (see CW spectrum in Fig. 4), which corresponds to the passband of gate 3. We note that similar switching behavior has been observed in the CCW direction. These results illustrate that the wavelength of the device can indeed be tuned by changing the currents injected in the SOA gates

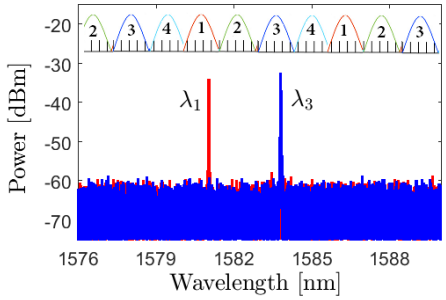

Fig. 4. Spectrum of the SRL's output in the CW direction when pumping the SRL at 95 mA, gate 1 at 14.2 mA and gate 3 either at 3.55 mA (red) or at 38 mA (blue). A schematic representation of the AWG channels passbands is plotted at the top.

In order to measure the wavelength switching speed, we apply a square wave signal to gate 1. This signal, with a period of 2.56 μs and a peak to peak voltage amplitude V_{pp}, is generated using an arbitrary waveform generator (Tektronix-AWG 520) and is added to the DC bias current using a bias-T. The device's output in the CCW direction is amplified using an external semiconductor optical amplifier (Thorlabs LM14S2) in order to ensure accurate measurements of the switching time, and then spectrally filtered using a tunable optical bandpass filter (Santec OTF-320 with 3 dB bandpass width of 0.5 nm) in order to select a particular LM in the measurement. Finally the time traces are recorded using a 2.4 GHz bandwidth detector connected to a 4 GHz bandwidth oscilloscope (Tektronix CSA7404). An Ando AQ6317B optical spectrum analyzer is used to measure the optical spectrum in the CW direction.

In Fig. 5(a), we show the driving square wave signal sent to gate 1 when the square-wave amplitude V_{pp} is set to 0.4 V. We set the laser bias current at 95 mA, the bias current of gate 3 at 7.81 mA, the bias current of gate 1 at 30.1 mA and the central frequency of the tunable filter at λ_1. In Fig. 5(b) we show the measured time trace of the intensity (at λ_1 because of the filter) in the CCW direction. This time trace clearly shows that the wavelength switches with the same periodicity as the modulation signal. When the signal sent to gate 1 [see Fig. 5(a)] is high, the device output at λ_1 [see Fig. 5(b)] is on. When the signal sent to gate 1 is switched to a low value, the device output at λ_1 switches off. Repeating these measurements, but with the tunable filter centered at λ_3 (not shown), shows that λ_3 is switched completely off when λ_1 is switched on. In order to estimate the wavelength switching speed, we assume that a switch is completed once the LM's power reaches 90% of the final level. Therefore, we define the transition time as the time it takes for a LM to go from 10% to 90% of its final power level. The time trace shown in Fig. 5(b) corresponds to an average transition time of 6 ns for both the rising and the falling edge of the modulation signal, which agrees with the results that we described earlier in [27]. However, as can be seen in Fig. 5(c), there is also a non-negligible delay (92 ns) between the trigger signal from the arbitrary waveform generator and the start of the switching transition. This delay time is not constant, but varies from one switching event to another. In order to deduce

OSA CONTINUUM

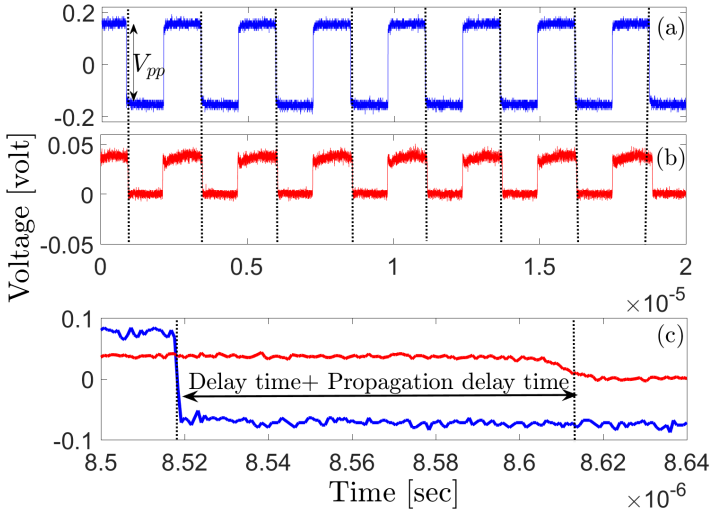

Fig. 5. (a) Trigger signal from arbitrary waveform generator to the oscilloscope. (b). Device output signal when the tunable bandpass filter is centered at λ_1. (c). Zoom in of a single switching event.

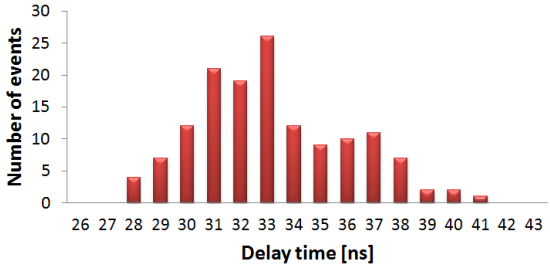

Fig. 6. Histogram of the wavelength switching's delay time at the falling edge of the gate 1 modulation using $V_{pp} = 0.5$ volt.

the delay time from the measured oscilloscope time traces, we have to take into account that there is propagation delay between the trigger signal and the signal reaching the optical detector. This delay depends on the cabling used in the setup and has been determined to be 50 ns for the setup used here. We take this delay into account by subtracting it from each delay measurement. For an accurate estimation of the wavelength switching delay, we also subtract the RC time constant of the on-chip SOA gates from the measured delay. This RC time constant has been measured to be around 10 ns. It is worth to mention that we did not notice any directional switching associated with the wavelength switching which takes place in the two directions simultaneously.

In Fig. 6, we show a histogram of the wavelength switching delay at the falling edge of the modulation signal in Fig. 5(a), taking into account 143 switching events and subtracting both the RC time constant and the cabling propagation delay. This histogram shows a quasi-Gaussian distribution in the delay time with an average of 31.7 ns and standard deviation of 4 ns. This delay time is clearly longer than the transition time.

Next, we study the effect on the transition and delay time of the modulation amplitude of the switching driving signal. We change the amplitude V_{pp} of the square wave signal which is applied on gate 1. In Fig. 7(a), we show the transition time as a function of V_{pp} where we can see that the transition time decreases from 13.3 ns to 2.3 ns when V_{pp} increases from 0.16 V

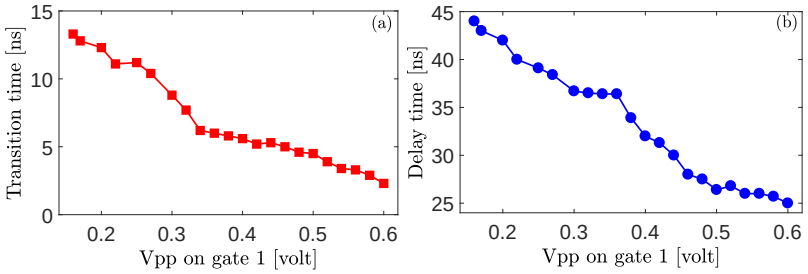

Fig. 7. (a). Transition time as function of V_{pp}. (b). Delay time as function of V_{pp}. Other experimental settings are I_{SRL}= 95 mA, I_1 =27.86 mA and I_3 =5.18 mA.

to 0.6 V. As the delay time changes stochastically, we measure a histogram of the delay time for each value of V_{pp}. We extract the mean value of the delay time from the histogram's data. We show in Fig. 7(b) the delay time as function of the modulation amplitude. The delay time decreases from 44 ns to 25 ns when V_{pp} increases from 0.16 V to 0.6 V. These results show that both the transition time and the delay time decrease by increasing V_{pp}.

4. Numerical simulations using travelling wave model and analysis

To get a better understanding of the wavelength switching we perform numerical simulations of the considered ring laser device using a traveling wave model (TWM) which has been introduced and used in several studies [29–32].

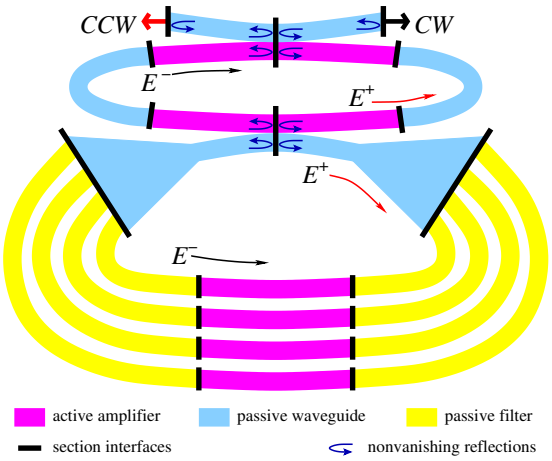

Fig. 8. Schematic representation of the simulated SRL with four FOF branches. Different colored frames and black segments indicate three different types of SRL sections and interfaces between these sections, respectively. Blue curved arrows represent all nonvanishing field reflections at these interfaces.

According to our modeling approach, the SRL with FOF branches is modelled as a set of mutually interconnected sections such as active amplifiers, passive waveguides, and passive wavelength filters, see Fig. 8. Whereas field transmission and reflection conditions at the interfaces of the adjacent sections realize coupling between different parts of the SRL, the TWM equations govern the dynamics of optical fields and carriers within each such part. Such modeling allows us on one hand to follow the transient dynamics in each of the LMs and in the corresponding carrier density, hence clarifying their role in the wavelength switching process. On the other

OSA CONTINUUM

hand, we investigate the effect of the different phase factors within the filtering branch on the switching process numerically which was difficult to be investigated experimentally.

4.1. Mathematical model

Our mathematical model is based on the TWM equations for the slow envelopes of the counterpropagating complex optical field amplitudes $E^+(z,t)$ and $E^-(z,t)$,

$$\frac{1}{v_g}\partial_t E^\pm \pm \partial_z E^\pm = \left(-i\beta^\pm(N,|E^\pm|^2) - \mathcal{D}\right) E^\pm + F^\pm_{sp}, \tag{1}$$

where v_g denotes the group velocity, z represents a unique spatial coordinate in the considered SRL device (including the outcoupling waveguide and FOF branches), whereas t is the time coordinate. The linear operator $\mathcal{D}$ models (relatively weak) material gain dispersion in the amplifying parts of the SRL as well as strong optical filtering within the passive waveguide part of each FOF branch. In the frequency (wavelength) domain, this operator is determined by a Lorentzian function with certain peak frequency, width, and amplitude [32]. The propagation factor $\beta^\pm$ is composed from the fixed static and dynamically changing parts,

$$\beta^\pm = \left[\delta - i\frac{\alpha_0}{2}\right] + \left[\alpha_H + \frac{i}{1+\varepsilon_s|E^\pm|^2+\varepsilon_c|E^\mp|^2}\right]\frac{g(N)}{2}. \tag{2}$$

The detuning factor δ and the nonradiative loss factor α_0 are responsible for the complex field phase shift and the field attenuation within each part of the considered SRL device. In the amplifying parts of the SRL device, β depends on the local carrier density $N(z,t)$ and, through the self- and cross-gain saturation, on the photon densities $|E^+|^2$ and $|E^-|^2$ within corresponding waves. Here, α_H and $g(N)$ are the linewidth enhancement factor and the logarithmic gain function, respectively. The dynamics of $N(z,t)$ is governed by the rate equations

$$\partial_t N = \frac{I}{qV} - R(N) - G\left(N,|E^\pm|\right), \tag{3}$$

where functions R and G denote spontaneous and stimulated recombination, respectively, q is the elementary charge, whereas I and V are the bias current and the volume of the active zone in the corresponding amplifying part of the SRL. To close the model, we need also to define field scattering relations at the interfaces of different parts of the SRL. In all nontrivial cases (facets of the waveguide, couplers of the ring and the outer waveguide, beam splitting and collecting at the AWG), the relations between the incident and scatterd fields are given by constant scattering matrices. In particular, we account for nonvanishing (asymmetric) field backscattering at the facets of the outcoupling waveguide (10^{-4} and 10^{-2} power reflection at the cw and ccw output facets, respectively) as well as 0.25×10^{-4} field power reflection at two positions representing localized couplers between SRL and two adjacent waveguides, see small curved arrows at these interfaces in Fig. 8. For more details on the model equations, scattering relations and model parameters, see Refs. [32, 33].

As it was briefly discussed in Ref. [33], the operation of the SRL device is sensitively depending not only on the bias current at the SRL and the different gate contacts, but also on the hardly identifiable phase relations (distinguishable by modulus 2π) within SRL and the FOF branches, $\varphi \sim \delta$. Thus, in order to mimic the experimental results discussed above and to explain the observed dynamics, we need to work in five- or even six-dimensional parameter space (including modulation amplitude and bias of the SRL).

4.2. Simulations of the gate switching

We start our numerical study from the conditions used in Fig. 8 of Ref. [33]. In this case, the proper choice of the bias currents in the 1-st and 3-rd channels has allowed achieving a stable

OSA CONTINUUM

simultaneous operation of two different-channel modes emitted in the CW direction. This is illustrated in Fig. 9(a) and 9(b), for which the bias currents at the gates of these channels were set to $I_1 = 29\,\mathrm{mA}$ and $I_3 = 18\,\mathrm{mA}$ ($I_2 = I_4 = 0$), whereas the corresponding static phase factors were set to zero, $\varphi_1 = \varphi_3 = 0$. In Fig. 9(a), it can be seen that the power for the 1-st and 3-rd channels are stable and almost fixed in time. In Fig. 9(b) where the wavelength relative to a central wavelength $\lambda_0 = 1.58\,\mu\mathrm{m}$ is plotted, one can see that the emitted LMs are indeed spectrally aligned with the filter passbands of channel 1 and 3. We expect that some increase/decrease of the bias within one of the activated branches will lead to the growth/decay of this channel mode and simultaneous decay/growth of the other channel modes. This assumption is supported by our simulations shown in panels (c) and (d) of the same figure. Here, we gradually increase one gate current (i.e. I_1 in panel (c) and I_3 in panel (d)) whereas the bias of another gate was kept constant [$I_3 = 18\,\mathrm{mA}$ in (c) and $I_1 = 29\,\mathrm{mA}$ in (d)]. Both these diagrams show that changing the gate current by 2 [panel (c)] or 5 [panel (d)] mA can be sufficient for achieving full switching between the different channels.

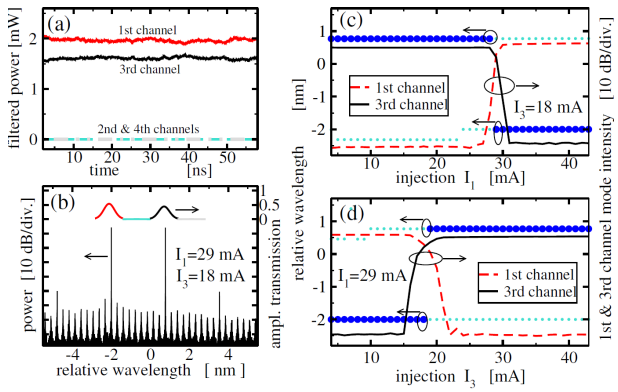

Fig. 9. Simulated SRL operation for continuous pumping of the 1st and 3rd gates. (a): time trace of the emitted CW field after filtering it with digital filters centred at the dominant first and third gate mode wavelengths. (b): optical spectra of this field (bottom) and different gate transmission spectra (above). (c): wavelengths of the dominant (large bullets) and the largest side (small bullets) modes within the two considered gates, and power of the emitted CW field after filtering it with digital filters as functions of I_1. (d): same as the previous panel as functions of I_3. In all cases, $\varphi_j = 0$, $j = 1, \ldots, 4$.

In our following simulations, we have studied the behavior of the SRL when one of the gate currents $I_1 = 29\,\mathrm{mA}$ or $I_3 = 18\,\mathrm{mA}$ is modulated with a time-periodic current

$$\delta I = \frac{a}{2} \cdot \mathrm{sign}\left(\sin(2\pi t/T)\right). \tag{4}$$

As it was predicted by Fig. 9, a large enough modulation amplitude a and period T imply a periodic switching between the modes of channel 1 and 3. Several typical current modulation-induced channel mode switchings are shown in Fig. 10 for different modulation amplitudes. At the left and right hand side of Fig. 10, we distinguish the transitions when the modulation current instantaneously decreases at time $t = 50\,\mathrm{ns}$ (left part of all panels) and increases at $t = 100\,\mathrm{ns}$ (right sides of the panels). To distinguish the evolution of separate longitudinal modes within each of the two considered channels, we apply six different digital Lorenzian filters to the calculated CW emission. The peak wavelengths of these filters correspond to the wavelengths of three first-channel and three third-channel modes, whereas the considered 0.2 nm bandwidth of these filters allows distinguishing different modes within the same channel.

OSA CONTINUUM

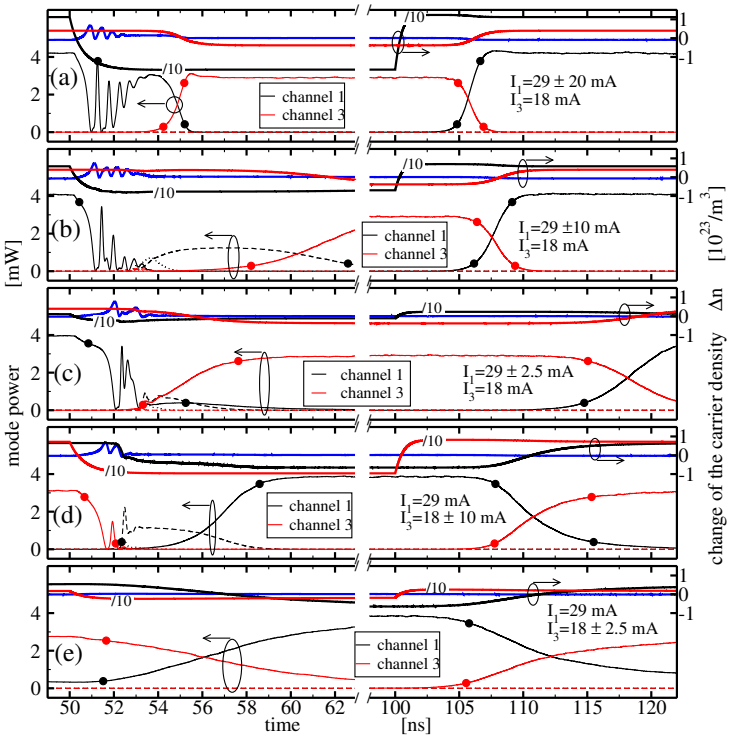

Fig. 10. Switchings between channel 1 and channel 3 modes by modulating the first gate with $a = 40\,\mathrm{mA}$ (a), 20 mA (b) and 5 mA (c), or by modulating the third gate with $a = 20\,\mathrm{mA}$ (d) and 5 mA (e). Modulation period in all cases was $T = 100\,\mathrm{ns}$. Black and red represent the first and the third gates, respectively. Thin: intensities of the central (solid), shorter-wavelength neighbor (dashed) and the longer-wavelength neighbor (dotted) mode within the first and third gates. Black and red bullets indicate beginning and end of the corresponding gate opening and closing. Thick: deviations of the mean carrier density within the ring (blue), within gate 1, and within gate 3 from the steady state densities $\bar{n}_R = 1.08 \cdot 10^{24}/m^3$, $\bar{n}_1 = 2.85 \cdot 10^{24}/m^3$, and $\bar{n}_3 = 2.03 \cdot 10^{24}/m^3$, respectively. Carrier density deviations within modulated gates are shown after dividing them by factor 10. The steady parts of the bias currents are $I_1 = 29\,\mathrm{mA}$ and $I_3 = 18\,\mathrm{mA}$.

Just after the decrease of the gate current, the current density in the corresponding gate amplifier (thick solid curves), the gate amplification, and the gate mode intensity are going down. In the cases (a)–(d), this rather strong perturbation of the dynamical state of the SRL after 1-2 ns also implies several relaxation oscillations, visible in Fig. 10 for example in the oscillations of the carrier density in the main SRL (thick blue solid curve) and the intensity of the former dominant mode of the modulated channel (thin solid curves). In the case (a), these oscillations last around four ns until the central third-channel mode replaces the former dominant first-channel mode.

In the cases (b) and (c), the perturbations of the operating state when I_1 is decreased excite earlier suppressed channel modes neighboring the initially dominant mode (see black thin dashed and dotted curves), which can contain some substantial part of the overall emission intensity for more than ten ns, see panel (b), before the other channel mode takes over and the wavelength switching is completed. A different situation is observed in the case (d), where the third gate was modulated. In contrast to the previously discussed cases (b) and (c), the perturbation now strongly excites side modes of the unmodulated channel 1, see thin black dotted and dashed curves in panel (d), whereas the side modes of the modulated channel remain well damped. This example

OSA CONTINUUM

also confirms an asymmetry in the action of the channels 1 and 3. We believe that this asymmetry could be changed by a suitable selection of the SRL current or the phase factors φ within the first and third channels. Finally, in the case (e), the current modulation induced perturbation is weak and implies neither relaxation oscillations nor significant changes of the carrier densities in the SRL and the gates. The intensity exchange between the two different channel modes is monotonous and smooth but takes more than ten ns. This long transition time is mainly induced by the small difference in the damping/amplification of the two involved channel modes.

In contrast, the switching between different channel modes shown in Fig. 10 when increasing the current of modulated gate at $t = 100$ ns is regular in all cases shown in Fig. 10. The exchange of the mode intensity is similar to the one of case (e) discussed above, i.e., the transition is smooth and the transition time depends mainly on the damping/amplification of the involved modes.

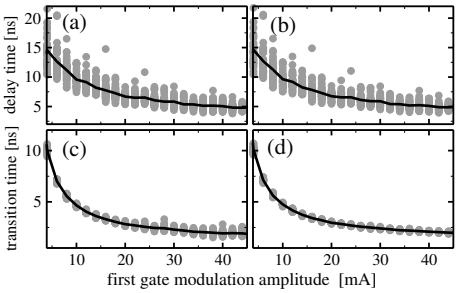

Fig. 11. Simulated gate switching delay-[(a), (b)] and transition- [(c), (d)] times as functions of the amplitude of the current modulation in the first gate. Switching on of the first gate and switching off of the third gate are considered in panels (a),(c) and (b),(d), respectively. Gray dots and black lines at each bias modulation amplitude represent these times in 40 individual calculations and the mean value of these times, respectively. The steady parts of the bias currents are the same as in Fig. 10.

In Fig. 11, we give an estimation of the channel switching delay and transition time and how they depend on the gate current modulation amplitude. The delay is determined as the time interval between changing the gate current and the last moment at which the intensity of an opening (closing) channel has reached 10% (90%) of the field intensity of this channel, respectively. The transition times shown in Fig. 9 are the time intervals required for the intensity transition between 10% and 90% levels of the corresponding channel emission power. The beginning and the end of these transitions are also indicated by thick bullets in Fig. 4. Since in our simulations multiple crossings of the 10% and 90% intensity levels were possible [see, e.g., left parts of Fig. 4(a) and 4(b)], for definition of the transition time intervals we use the last of these crossings. We note that in contrast to the calculations of Fig. 10, in Fig. 11 we are not trying to distinguish between different modes in the same channel, but, similarly to Fig. 9(a), we are inspecting the overall contributions of the first and third channels to the total CW emission. Left and right panels of Fig. 11 represent switching on of the first channel and switching off of the third channel when modulating the first gate current. These diagrams generalize our simulations represented in the right parts of Fig. 10(a), 10(b), and 10(c), where the black and red thin curves were showing the evolution of the first [see Fig. 11(a)] and the third [Fig. 11(b)] channel modes.

The diagrams of Fig. 11 correspond to a regular smooth intensity exchange between the different channel modes at rising edge of the modulated gate current (see right sides of all panels in Fig. 10). The increasing modulation amplitude implies a growing contrast between the amplification/damping of the two involved modes and, consequently, results in a faster exchange of these states. The transition times for the modulated and unmodulated channel modes (left and right panels in Fig. 11) are rather similar in this case.

OSA CONTINUUM

The limiting factors for the switching speed are not only the (short) photon life time, but also (not so short) carrier relaxation time. First, after switching of the current, one needs some finite time before the gate is fully opened or fully closed, and this time is comparable with the laser switching-on or laser switching-off time, i.e., one or more ns. This initial transition can be seen in Fig. 10, see behavior of the upper solid curve in panels (a)-(c) and upper red solid curve in (d) and (e). Obviously, larger modulation amplitude we use - longer transient time can be seen. Second, some transient time is needed for the transitions of the carrier density of laser and gate 3 from the situation before the switching to the situation after the switching. In general, these transitions are initiated a bit later, when the field is starting to "flow" through the previously closed gate (i.e., when a gate is already opened) and the flow of the field through another gate is diminished. For some cases, the transition for the carrier density of the laser is finished only after several rounds of relaxation oscillations (panels a-d), what is another reason of the prolongated switching procedure. Third reason is the relation between damping/amplification of the two main in the switching involved modes. Even though the damping/growth are exponential, the difference between these exponential factors can be rather low (especially if small modulation amplitude is applied, see panel e), In this case, the exchange of the field intensity in the two modes can be rather long.

4.3. *Impact of the field phase relations*

The situation, however, becomes different once we choose other values of the static phase factors φ_1 and φ_3 of the FOF. Figure 12 presents several sets of simulations, similar to those considered in Fig. 9(c) and 9(d), performed for different phases φ_1 and φ_3, fixed current I_3 (or I_1) and tuned current I_1 (or I_3). We should mention that the currents of the gates are not modulated in this and the following calculations.

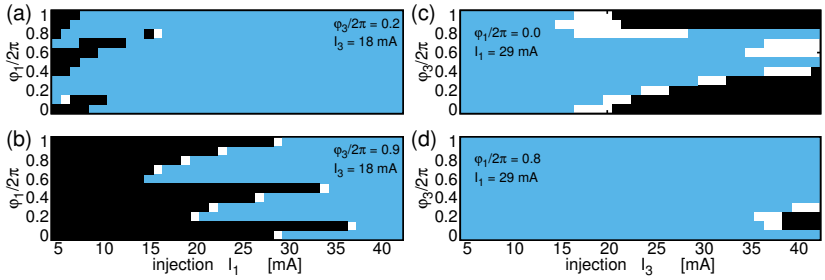

Fig. 12. Simulated dominance of the first channel modes (light shading), third channel modes (black), and dual gate operation with < 10 dB suppression of the weaker channel mode (white) for different φ_1 and I_1 whereas $I_3 = 18$ mA and $\varphi_3/2\pi = 0.2$ (a) or $\varphi_3/2\pi = 0.9$ (b), as well as different φ_3 and I_3 whereas $I_1 = 29$ mA and $\varphi_1 = 0$ (c) or $\varphi_1/2\pi = 0.8$ (d).

The panels (a) and (b) of Fig. 12 indicate the dominant channel mode when the first gate bias current I_1 is tuned for each considered phase φ_1 (the different horizontal crossections of Fig. 12 (a) and (b) correspond to different values of the phase φ_1). The simulations were performed for a fixed third gate current $I_3 = 18$ mA and phase φ_3, which was $0.2 \cdot 2\pi$ and $0.9 \cdot 2\pi$ in the panels (a) and (b) respectively.

We can see that in both cases the current I_1 where the switching between channels from Fig. 12 takes place (vertical interfaces between light and black shadings) depends in a non-monotonous manner on the factor φ_1. Second, in the absence of phase control, even 30 mA steps of I_1 can be not enough to realize switching between two channels: the first channel mode can already be dominant for small $I_1 \approx 5$ mA, see panel (a), whereas, for particular values of the phases, I_1 as large as 35 mA still cannot prevent the dominance of the third channel mode, see panel (b).

OSA CONTINUUM

It is noteworthy, that even though a sufficient strong I_1 usually imposes the dominance of the first- channel modes and the suppression of the third- channel modes, we can also find conditions where the closed third channel can be reopened again at even higher I_1, see, e.g., a reappearing black region at $\varphi_1/2\pi = 0.8$ in Fig. 12(a). This behavior is again resulting from the complex field phase relations: the growth of the carrier density in a gate when increasing that gate's current imposes not only the growth of the field amplification but also imposes changes in the refractive index, i.e., the reduction of the overall phase factor $\sim \Re\beta$ in the first channel, which is of crucial importance in the considered lasers.

A similar situation can be observed when the first gate phase φ_1 and the bias $I_1 = 29\,\mathrm{mA}$ are kept constant, whereas I_3 is tuned for each value of φ_3, see panels (c) and (d) of the same figure calculated for $\varphi_1 = 0$ and $0.8 \cdot 2\pi$, respectively. In this case, of course, the first and the third channel modes dominate for smaller and larger I_3, respectively.

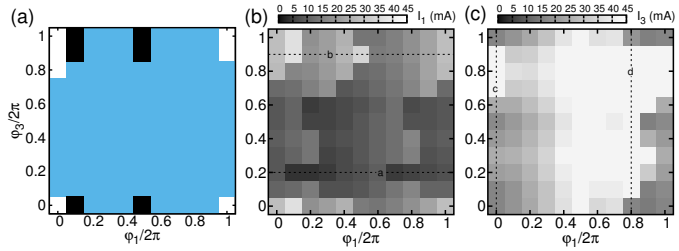

Fig. 13. Study of the phase factors φ_1 and φ_3. (a): the first (light shading), third (black), or dual (white) channel mode operation for $I_1 = 29\,\mathrm{mA}$ and $I_3 = 18\,\mathrm{mA}$. (b): the first gate bias I_1 giving the upper border of the third channel mode operation regime once $I_3 = 18\,\mathrm{mA}$. (c): the third gate bias I_3 giving the upper border of the first channel mode operation regime once $I_1 = 29\,\mathrm{mA}$. Horizontal and vertical dashed lines in panels (b) and (c) correspond to the simulations presented in panels (a),(b) and (c),(d) of Fig. 12, respectively.

Another representation of our calculations for arbitrary combinations of phase factors (φ_1, φ_3) is given in Fig. 13. Panel (a) of this figure indicates which mode is dominant for different values of φ_1 and φ_3 when the gate bias currents are fixed at $I_1 = 29\,\mathrm{mA}$ and $I_3 = 18\,\mathrm{mA}$. The simulations results plotted in Fig. 9(a) show that for most-but not all- combinations of φ_1 and φ_3, the first (stronger pumped) channel mode dominates the output of the laser. The situation considered in Fig. 9(a) and 9(b) using $(\varphi_1, \varphi_3) = (0, 0)$ is represented by white (dual-gate-operation) areas at the corners of this diagram.

Figure 13(b) represents the results of multiple simulations when increasing I_1 whereas $I_3 = 18\,\mathrm{mA}$ is fixed. This diagram indicates the smallest critical value $I_1^c(\varphi_1, \varphi_3)$ that makes the first channel dominant. Two dashed horizontal lines "a" and "b" denote the values of φ_3 at which the smallest and largest values of I_1^c were obtained and correspond to the simulations represented in panels (a) and (b) of Fig. 12, respectively. Similarly, Fig. 13(c) shows critical $I_3^c(\varphi_1, \varphi_3)$ obtained during simulations with increasing I_3 whereas $I_1 = 29\,\mathrm{mA}$. The vertical dashed lines "c" and "d" correspond to the panels (c) and (d) of Fig. 12. Once again, in both these panels, we note a large difference between the smallest and largest critical currents I_1^c (or I_3^c). This large range can cause troubles when trying to switch between different channels. Namely, a moderate current modulation amplitude cannot guarantee a successful switching between the channels for an arbitrary choice of the phase factors.

5. Conclusion

We have investigated the wavelength switching features of a SRL that uses FOF as wavelength tuning mechanism. The switching time is composed of a sum of the delay and transient times. We

OSA CONTINUUM

have experimentally showed a wavelength transition time of a few nano seconds and a substantial delay time. Both the transition and delay times depend on the modulation amplitude applied to the SOA gate in the feedback loop.

The numerical results using TWM have shown that the channel switching behavior is sensitively depending not only on the selection of the gate current modulation amplitude, but also on the fixed currents of the two selected channels, on the bias of the SRL itself, and on different phase relation factors φ within the filtering branches and the SRL. The undesired long transient time when one gate is switched off will be further investigated in a future work.

To improve the state switching performance, we have to control the field phase relations within separate filtering branches, e.g., by introducing additional phase-control sections [34, 35] within these branches. To accelerate the wavelength switching time, we need to have a faster carrier relaxation time within the gates (gate amplifiers on the basis of quantum dots or gates consisting of (saturated or unsaturated) saturable absorbers nearby the well pumped amplifiers) and to find a situation, where a small change of the field transmission through the branch implies a large change of the related channel mode gain/damping (larger differential gain in the gates or possible exploitation of phase conditions and nonlinearities). To improve the symmetry between different channels (to equalize the detuning between the central channel mode and the channel filter peak wavelengths), a slight change of the SRL length or the AWG spectral range could also be useful.

Funding

Belgian FWO; Hercules Foundation; Research Council of the VUB; Technical University of Moldova (projects 14.02.116F/34S and 16.80012.02.27F); FWO by ways of EOS Project G0F6218N (EOS ID 30467715).

Acknowledgement.

The authors thank X.J.M. Leijtens and J. Bolk from TUE for device fabrication in the framework of JePPIX. M.R. acknowledges being a Faculty of Science and Engineering Visiting Researcher in the Department of Physics and Astronomy at Macquarie University, Sydney, Australia, when part of this research was undertaken.

References

1. J. Buus and E. J. Murphy, "Tunable lasers in optical networks," J. Lightwave Technol. **24**, 5–11 (2006).
2. F. Kong, B. Romeira, J. Zhang, W. Li and J. Yao, "A dual-wavelength fiber ring laser incorporating an injection-coupled optoelectronic oscillator and its application to transverse load sensing," J. Lightwave Technol. **32**, 1784–1793 (2014).
3. N. J. C. Libatique and R. K. Jain, "Precisely and rapidly wavelength-switchable narrow-linewidth 1.5-μ m laser source for wavelength division multiplexing applications," IEEE Photon. Technol. Lett. **11**, 1584–1586 (1999).
4. L. A. Coldren, "Monolithic tunable diode lasers," IEEE J. Sel. Top. Quantum Electron. **6**, 988–999 (2000).
5. Y. Tachikawa and K. Okamoto, "Arrayed-waveguide grating lasers and their applications to tuning-free wavelength routing," IEE Proc. Optoelectron. **143**, 322–328 (1996).
6. A. P. A. Fischer, O. K. Andersen, M. Yousefi, S. Stolte, and D. Lenstra, "Experimental and theoretical study of filtered optical feedback in a semiconductor laser," IEEE J. Quantum Electron. **36**, 375–384 (2000).
7. J. Zhao, D. Lenstra, R. Santos, M. J. Wale, M. K. Smit, and X. J. M. Leijtens, "Stability of a monolithic integrated filtered feedback laser," Opt. Express **20**, B270–B278 (2012).
8. G. Verschaffelt and M. Khoder, "Directional power distribution and mode selection in micro ring lasers by controlling the phase and strength of filtered optical feedback," Opt. Express **26**, 14315–14328 (2018).
9. B. Docter, J. Pozo, S. Beri, I. V. Ermakov, J. Danckaert, M. K. Smit, and F. Karouta, "Discretely tunable laser based on filtered feedback for telecommunication applications," IEEE J. Sel. Top. Quantum Electron. **16**, 1405–1412 (2010).
10. S. Fürst, S. Yu, and M. Sorel, "Fast and digitally wavelength-tunable semiconductor ring laser using a monolithically integrated distributed Bragg reflector," IEEE Photon. Technol. Lett. **20**, 1926–1928 (2008).
11. M. Sorel, J. P. R. Laybourn, A. Scirè, S. Balle, G. Giuliani, R. Miglierina, and S. Donati, "Alternate oscillations in semiconductor ring lasers," Opt. Lett. **27**, 1992–1994 (2002).
12. N. Li, W. Pan, S. Xiang, B. Luo, L. Yan, and X. Zou, "Hybrid chaos-based communication system consisting of three chaotic semiconductor ring lasers," Appl. Opt. **52**, 1523–1530 (2013).

OSA CONTINUUM

13. S. Sunada, T. Harayama, K. Arai, K. Yoshimura, K. Tsuzuki, A. Uchida, and P. Davis, "Random optical pulse generation with bistable semiconductor ring lasers," Opt. Express **19**, 7439–7450 (2011).
14. T. Pérez, A. Scirè, G. Van der Sande, P. Colet, and C. Mirasso, "Bistability and all-optical switching in semiconductor ring lasers," Opt. Express **15**, 12941–12948 (2007).
15. G. Yuan and S. Yu, "Bistability and switching properties of semiconductor ring lasers with external optical injection," IEEE J. Quantum Electron. **44**, 41–48 (2008).
16. A. Trita, G. Mezosi, M. Sorel, and G. Giuliani, "All-optical toggle flip-flop based on monolithic semiconductor ring laser," IEEE Photon. Technol. Lett. **26**, 96–99 (2013).
17. M. T. Hill, H. J. S. Dorren, T. de Vries, X. J. M. Leijtens, J. H. den Besten, B. Smalbrugge, Y. S. Oei, H. Binsma, G. D. Khoe, and M. K. Smit, "A fast low-power optical memory based on coupled micro-ring lasers," Nature **432**, 206–209 (2004).
18. S.-S. Li, V. Pusino, S.-C. Chan, and M. Sorel, "Experimental investigation on feedback insensitivity in semiconductor ring lasers," Opt. Lett. **43**, 1974–1977 (2018)
19. M. Sorel, P. J. R. Laybourn, G. Giuliani, and S. Donati, "Unidirectional bistability in semiconductor waveguide ring lasers," Appl. Phys. Lett. **80**, 3051–3053 (2002).
20. G. Morthier and P. Mechet, "Theoretical analysis of unidirectional operation and reflection sensitivity of semiconductor ring or disk lasers," IEEE J. Quantum Electron. **49**, 1097–1101 (2013).
21. M. Khoder, "Longitudinal modes competition in micro ring laser subject to both self and cross optical feedback," Commun. Nonlinear Sci. Numer. Simul. **62**, 146–156 (2018)
22. M. Khoder, G. Van der Sande, and G. Verschaffelt, "Reducing the sensitivity of semiconductor ring lasers to external optical injection using selective optical feedback," J. Appl. Phys. **124**, 133101 (2018).
23. I. V. Ermakov, S. Beri, M. Ashour, J. Danckaert, B. Docter, J. Bolk, X. J. M. Leijtens, and G. Verschaffelt, "Semiconductor ring laser with on-chip filtered optical feedback for discrete wavelength tuning," IEEE J. Quantum Electron. **48**, 129–136 (2012).
24. M. Khoder, G. Verschaffelt, R. M. Nguimdo, J. Bolk, X. J. M. Leijtens, and J. Danckaert, "Controlled multiwavelength emission using semiconductor ring lasers with on-chip filtered optical feedback," Opt. Lett. **38**, 2608–2610 (2013).
25. M. Khoder, G. Verschaffelt, R. M. Nguimdo, J. Bolk, X. J. M. Leijtens, and J. Danckaert, "Digitally tunable dual wavelength emission from semiconductor ring lasers with filtered optical feedback," Laser Phys. Lett. **10**, 075804 (2013).
26. M. Khoder, G. Van der Sande, J. Danckaert, and G. Verschaffelt, "Effect of external optical feedback on tunable micro-ring lasers using on chip filtered feedback," IEEE Photon. Technol. Lett. **28**, 959–962 (2016).
27. M. Khoder, R. M. Nguimdo, J. Bolk, X. J. M. Leijtens, J. Danckaert, and G. Verschaffelt, "Wavelength switching speed in semiconductor ring lasers with on-chip filtered optical feedback," IEEE Photon. Technol. Lett. **26**, 520–523 (2014).
28. X. J. M. Leijtens, "JePPIX : the platform for indium phosphide-based photonics," IET Optoelectron. **5**, 202–206 (2011).
29. J. Javaloyes and S. Balle, "Emission directionality of semiconductor ring lasers: a traveling-wave description," IEEE J. Quantum Electron. **45**, 431–438 (2009).
30. A. Perez-Serrano, J. Javaloyes, and S. Balle, "Multichannel wavelength conversion using four-wave mixing in semiconductor ring lasers," IEEE Photon. Technol. Lett. **25**, 476–479 (2013).
31. A. Perez-Serrano, J. Javaloyes, and S. Balle, "Directional reversals and multimode dynamics in semiconductor ring lasers," Phys. Rev. A **89**, 023818 (2014).
32. M. Radziunas, 'Traveling wave modeling of nonlinear dynamics in multisection semiconductor laser diodes," in *Handbook of Optoelectronic Device Modeling and Simulation: Lasers, Modulators, Photodetectors, Solar Cells, and Numerical Methods*, J. Piprek, ed. (CRC Press, 2017), vol. 2, pp. 153–182.
33. M. Radziunas, M. Khoder, V. Tronciu, J. Danckaert, and G. Verschaffelt, "Tunable semiconductor ring laser with filtered optical feedback: Traveling wave description and experimental validation," J. Opt. Soc. Am. B **35**, 380–390 (2018).
34. M. Radziunas, H.-J. Wünsche, B. Sartorius, O. Brox, D. Hoffmann, K. Schneider, and D. Marcenac, "Modeling self-pulsating DFB lasers with an integrated phase tuning section," IEEE J. Quantum Electron. **36**, 1026–1034 (2000).
35. G. Verschaffelt, M. Khoder, and G. Van der Sande "Random number generator based on an integrated laser with on-chip optical feedback," Chaos **27**, 114310 (2017).